PHYSICAL REVIEW B **96**, 195104 (2017)

Observation of Volkov-Pankratov states in topological HgTe heterojunctions using high-frequency compressibility

A. Inhofer,[1] S. Tchoumakov,[2] B. A. Assaf,[3] G. Fève,[1] J. M. Berroir,[1] V. Jouffrey,[4] D. Carpentier,[4] M. O. Goerbig,[2] and B. Plaçais[1,*]

[1]*Laboratoire Pierre Aigrain, Ecole Normale Supérieure, PSL Research University, CNRS, Université Pierre et Marie Curie, Sorbonne Universités, Université Paris Diderot, Sorbonne Paris-Cité, 24 rue Lhomond, 75231 Paris Cedex 05, France*
[2]*Laboratoire de Physique des Solides, CNRS UMR 8502, Université Paris-Sud, Université Paris-Saclay, F-91405 Orsay Cedex, France*
[3]*Département de Physique, Ecole Normale Supérieure, PSL Research University, CNRS, 24 rue Lhomond, 75231 Paris Cedex 05, France*
[4]*Université Lyon, ENS de Lyon, Université Claude Bernard, CNRS, Laboratoire de Physique, F-69342 Lyon, France*

K. Bendias,[5] D. M. Mahler,[5] E. Bocquillon,[5,1] R. Schlereth,[5] C. Brüne,[5] H. Buhmann,[5] and L. W. Molenkamp[5]
[5]*Faculty for Physics and Astronomy and Röntgen Center for Complex Material Systems, Universität Würzburg, Am Hubland, D-97074 Würzburg, Germany*

(Received 21 March 2017; revised manuscript received 24 July 2017; published 1 November 2017)

It is well established that topological insulators sustain Dirac fermion surface states as a consequence of band inversion in the bulk. These states have a helical spin polarization and a linear dispersion with large Fermi velocity. We report on a set of experimental observations supporting the existence of additional massive surface states. These states are also confined by the band inversion at a topological-trivial semiconductor heterojunction. While first introduced by Volkov and Pankratov (VP) before the understanding of the topological nature of such a junction, they were not experimentally identified. Here we identify their signatures on transport properties at high electric field. By monitoring the ac admittance of HgTe topological-insulator field-effect capacitors, we access the compressibility and conductivity of surface states in a broad range of energies and electric fields. The Dirac states are characterized by a compressibility minimum, a linear energy dependence, and a high mobility persisting up to energies much larger than the transport band gap of the bulk. At higher energies, we observe multiple anomalous behaviors in conductance, charge metastability, and Hall resistance that point towards the contribution of massive surface states in transport scattering and charge transfer to the bulk. The spectrum of these anomalies agrees with predictions of a phenomenological model of VP states in a smooth topological heterojunction. The model accounts for the finite interface depth, the effect of electric fields including Dirac screening, and predicts the energy of the first VP state. The massive surface states are a hallmark of topological heterojunctions, whose understanding is crucial for transport studies and applications.

DOI: 10.1103/PhysRevB.96.195104

I. INTRODUCTION

Topological materials have emerged [1] as a new class of matter with properties arising from peculiar crystal properties. These include topological insulators (TIs) with band inversion due to, e.g., spin-orbit interaction [2,3], induced topological superconductors [1], and topological semimetals [4,5]. They have attracted much attention as hosts of exotic modes such as Majorana, Dirac, or Weyl fermions, depending on symmetry and dimensionality. Topology also leaves macroscopic footprints such as the quantum spin Hall effect in two-dimensional (2D) TIs [6], quantum Hall and Dirac screening in 3D TIs [7], the fractional Josephson effect in topological-insulator–semiconductor (TI-SC) junctions [8–10], and, more recently, the quantized Faraday rotation in 3D TIs [11,12].

In spite of intensive studies, some important questions remain. One concerns the robustness of the topological states in practical implementations for quantum or classical topological electronics. Another is the possibility of new members in the family of topological states and the related question of higher-energy excitations. Indeed, as predicted in Ref. [13], a limiting factor for the dynamics of Majorana braiding is the existence of surface states at higher energies. One may wonder if similar high-energy states accompany Dirac states in 3D TIs. Remarkably, this question has been anticipated theoretically by Volkov and Pankratov in Ref. [14] who considered topological heterojunctions (THJs) between inverted and noninverted $Pb_xSn_{1-x}Te$ semiconductors. They predicted the existence of both the helical Dirac ground state and a series of massive surface states, thereafter called Volkov-Pankratov states (VPSs). VPS theory is sketched below and detailed in Ref. [15] with the important addition of field effects. Some of the properties of a THJ will certainly depend on the existence of VPSs; let us mention the anomalous screening properties in 3D TIs reported in Ref. [7]. The present work aims at unveiling VP states and highlighting their role in transport by a high-frequency (rf) measurement of compressibility in high-mobility strained HgTe 3D TIs using a rf capacitor geometry, which is a building block of topological electronics.

The rf compressibility approach complements the angle-resolved photoemission spectroscopy (ARPES), which has proven very efficient in identifying Dirac states (see, e.g., Refs. [16–19]). Indeed, ARPES is not fully versatile as it is limited to vacuum-TI interfaces. It therefore excludes TI capping and gating, which turn out to be essential to detect VPSs as well as for future topological electronics. While massive surface states were reported for oxidized Bi_2Se_3 and Bi_2Te_3 samples

*bernard.placais@lpa.ens.fr

 ©2017 American Physical Society

[20,21], they were extrinsically induced by on-purpose surface doping. On the other hand, the transport technique is sensitive to buried interface states, even in the presence of capping and top gating, and is therefore well suited to map Dirac states and the VPSs in THJs. In fact, a signature of VPSs lies in their anomalous electric-field $\mathcal{E}$ response, coupled with the Dirac nature of states in a THJ; such an electric-field susceptibility can be regarded as a pseudomagnetic response with an effective magnetic field $\mathcal{E}/v_F$, where v_F is the velocity of Dirac carriers. With $\mathcal{E} \sim 10^8$ Vm^{-1} and $v_F \sim 10^6$ ms^{-1}, one has access to very large fields, $\mathcal{E}/v_F \sim 100$ T. Our technique is based on high-frequency compressibility measurements introduced in Ref. [22]. The device is a metal-insulator–TI field-effect capacitor (MITI-cap), with a metallic plate acting as a dc and rf gate and the THJ acting as a rf drain. The broadband admittance measures the differential capacitance per unit area $C(V_g)$ and the TI sheet conductivity $\sigma(V_g)$ as a function of the dc gate voltage V_g. From $C(V_g)$, we extract the carrier density $n(V_g)$, the quantum capacitance $C_Q(V_g)$, analog to the compressibility $\chi = \partial n/\partial\mu = C_Q/e^2$, from which we deduce the surface Fermi energy $\mu(V_g)$ that is essential for VPS spectroscopy. The joint measurement of σ and C_Q gives access to the diffusion constant $\mathcal{D}(\mu) = \sigma/C_Q$ used here as a spectroscopic tool of the surface states. Below the first VPS gap ($\mu \lesssim E_1$), we find $\mathcal{D} \propto \mu$ and a large mobility $\mu_e = 2\mathcal{D}/\mu \simeq 12$ m^2 V^{-1}s^{-1}, characteristic of the Dirac state. As chemical potential crosses the VPS1 band edge ($\mu \simeq E_1$), an efficient intersubband scattering sets in [23], which is responsible for a drop of $\mathcal{D}$. The scattering spectroscopy turns out to have a better resolution than compressibility itself, which is eventually blurred by residual heavy-hole bulk contributions in cubic HgTe.

A fundamental concern is the distinction between VPS and classical massive surface states such as reported in Refs. [20,21]. Indeed, both are massive, doubly degenerate, and occur at similar energies. The main distinction lies in the nature of confinement: relativistic VPSs are confined in an energy gradient, whereas classical states are trapped in a potential well involving electrostatic band bending. Experimentally, they can be distinguished by their electric-field sensitivity, as discussed below (Sec. IV) and in Ref. [15]: VPSs are redshifted, whereas trivial states are naturally blueshifted as a positive electric field enhances quantum confinement whereas a negative one destroys the well altogether. This anomalous field effect is linked to the existence of a critical field $\mathcal{E}_T = (\Delta_2 + \Delta_1)/e\xi$ at which VPSs collapse. As discussed in Ref. [15], it corresponds to the situation where the gap alignment between the trivial and topological regions closes. Here, $2\Delta_2$ ($-2\Delta_1$) are the positive (negative) band gaps of the direct (inverted) semiconductors, and ξ is the penetration depth of the Dirac state. $\mathcal{E}_T$ sets both the energy scale of the zero-field VPS subband series, $E_m(0) = \sqrt{2m\hbar v_F e\mathcal{E}_T}$ with m a positive integer, and the electric-field dependence $E_m(\mathcal{E}) = E_m(0)(1 - \mathcal{E}^2/\mathcal{E}_T^2)^{3/4}$. In particular, the $E_1(\mathcal{E})$ curve defines the phase boundary for Dirac screening. Taking $\xi \gtrsim \hbar v_F/\Delta_1 \simeq 5$ nm and $\Delta_1 \simeq \Delta_2/3 \simeq 0.15$ eV [24] for the CdHgTe/HgTe smooth THJs used in this work, the predicted critical field and VPS1 energy are $\mathcal{E}_T \lesssim 1.2\ 10^8$ Vm^{-1} and $E_1 \lesssim \Delta_1\sqrt{2(1 + \Delta_2/\Delta_1)} \simeq 0.4$ eV. Five signatures of the VPS are reported here: the observation of a Dirac-state scattering peak in undoped samples at an energy $E_1 \simeq 0.35$ eV close to the predicted value, the onset of a secondary type of carrier and Dirac screening breakdown at the same energy, the observation of three scattering peaks obeying the predicted VPS series $E_m = \sqrt{m}E_1$, and their electric-field redshift in oxide capped doped samples.

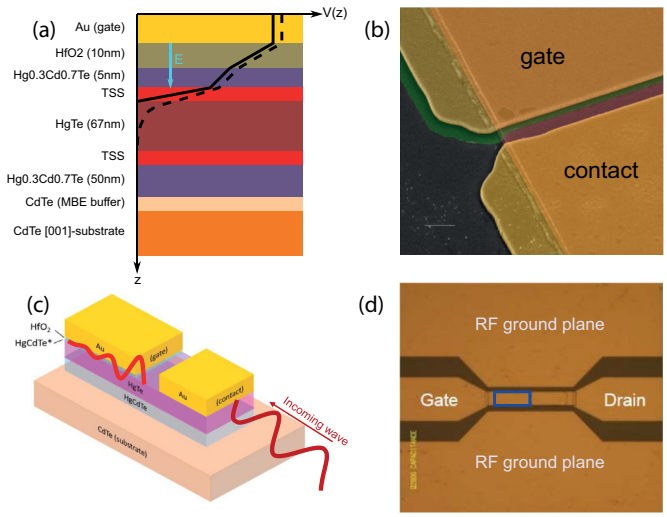

FIG. 1. Description of the MITI-caps. (a) Sketch of a HgTe/$Cd_{0.7}Hg_{0.3}$Te capped heterostructure. Also shown in the figure are sketches of the electrostatic potential across the structure in the case of Dirac screening (solid line) and a mixed surface/bulk state (BS) screening (dashed line). (b) Colored SEM picture at a capacitor edge showing the gate and contact metallizations (gold), the HgTe mesa (purple), and the HfO_2 insulating layer (green). (c) Sketch of the evanescent wave penetration of charge in the HgTe MITI-cap when driven at rf. (d) Optical image of the capacitor embedded in a coplanar wave guide. The 44×20 μm gated area is highlighted by a blue rectangle.

The paper is organized as follows. In Sec. II, we describe the experimental principles including the fabrication of high-mobility CdHgTe/HgTe THJs. Section III is a report of rf surface compressibility measured over a broad range of electric field in undoped and doped HgTe samples. Special attention is devoted to charge metastability effects and their relationship to VPSs. Observations are confirmed by control experiments performed in Hall bars with similar gate stacks. Section IV presents a heuristic model of the VPSs and their electric-field dependence, complemented by $k \cdot P$ numerical calculations. The comparison between theory and experiment in Sec. V supports the existence of VPSs in CdHgTe/HgTe topological heterojunctions. We conclude in Sec. VI with perspectives offered by the VPS for future topological electronics.

II. EXPERIMENTAL PRINCIPLES

The MITI-caps are based on high-mobility HgTe/CdHgTe heterostructures [Fig. 1(a)] grown by molecular-beam epitaxy [7,25,26] where the HgTe layer, of thickness $t_{HgTe} = 68$ nm, is strained by the CdTe insulating substrate so as to open a small band gap $\simeq$0.02 eV in the topological HgTe layer between the light-electron and heavy-hole Γ_8 bands. The gap is smaller than the light-electron light-hole (Γ_8-Γ_6) inverted band gap, $-2\Delta_1 = \Delta_{\Gamma_6-\Gamma_8} \simeq -300$ meV [27], responsible for the Dirac surface states. We use a wet-etching technique [28] to design a

mesa and optical lithography to deposit contacts and define the gated area of the capacitor. A gold gate electrode is evaporated on top of a 10-nm-thin HfO_2 insulating layer, grown by low-temperature atomic layer deposition (ALD) techniques. An ohmic contact, with a resistance $R_c \simeq 50$ Ohms, is deposited by Ge/Au evaporation. A false-color scanning electron microscopy (SEM) image of the gate-contact alignment is shown in Fig. 1(b). Two series of samples have been fabricated. Type-A samples (S_A) are covered by a 5 nm $Cd_{0.7}Hg_{0.3}Te$ capping layer protecting the HgTe during the process and providing a well-defined trivial insulator boundary of band gap $2\Delta_2^A \simeq 0.9$ eV [29,30] [Fig. 1(a)]. The total insulator thickness is $t_{\rm ins} = 15$ nm. Type-B samples (S_B) are devoid of a capping layer and HfO_2 is directly deposited on HgTe (not shown in the figure). This entails an unintentional electron doping of the HgTe bulk (density $n_0 \simeq 2.6\ 10^{12}$ cm^{-2}; see below). The HgTe-HfO_2 interface involves an oxidized HgTe insulating layer of unknown, and presumably small, band gap ($\Delta_2^B \ll \Delta_2^A$). We have characterized *in situ* the permittivity, $\varepsilon_{\rm HfO_2} \simeq 3.6$, of the thin oxide layer using a metal-oxide-metal (MOM) control capacitor. This value is process dependent and deviates here from the accepted bulk value $\varepsilon_{\rm HfO_2} \simeq 11.7$ [31]. Taking $\varepsilon_{CdHgTe} \simeq 8.5$ for the capping layer [29,30], we estimate the capacitance of our insulating stack $C_{\rm ins} = 2.65$ mF/m^2, in agreement with our measurement below. The MITI-caps are embedded in coplanar waveguides [Fig. 1(d)], designed for 0–40 GHz measurements. Five similar MITI-caps of varied dimensions are fabricated per chip complemented by MOM, dummy, and through-line structures used for calibration purposes (see below). For definiteness, experiments reported here refer to two capacitors of dimensions $L \times W = 44 \times 20\ \mu$m, one of type A and one of type B.

Compressibility measurements have been considered so far mainly for the characterization of Bi_2Se_3 thin crystals [32] and for the purpose of Landau-level spectroscopy in HgTe films [33]. Here we subtract the series combination of insulator capacitance $C_{\rm ins}$ to the total capacitance $C_{\rm tot}$ to obtain the quantum capacitance correction, $C_Q = e^2\chi$. $C_{\rm tot}$ can be tuned by a dc gate voltage V_g controlling altogether the charge density n and the applied electric field $\mathcal{E}$. High-frequency measurements ($\lesssim$10 GHz) give access to the dissipative regime, governed by the conductivity σ, and yield the diffusion constant $\mathcal{D} = \sigma/C_Q$. Thin insulators allow for high fields eventually exceeding the critical field $\mathcal{E}_T \simeq 1.2\ 10^8$ Vm^{-1} of our CdHgTe/HgTe THJs. Compressibility measurement plays an important role here. First, it provides an absolute chemical potential scale with a zero given by the Dirac dip, and second, it gives the precise behavior of the diffusion constant, which helps identify the scattering mechanisms.

Following earlier work on graphene [22], we primarily measure the electronic compressibility by vectorial network analyzer (VNA) techniques (frequency range $\omega/2\pi = 50$ kHz–8 GHz) in a cryogenic rf probe station at 10 K. Standard *in situ* calibration techniques enable one to de-embed the circuitry and the contact resistance contributions from the MITI-cap admittance $Y(\omega)$ of interest. The admittance spectrum $Y(\omega)$ is accurately described by a distributed resistance-capacitance model, $Y(\omega)/W = +\jmath C_{\rm tot}\omega L \times \tanh(\sqrt{\jmath\sigma^{-1}C_{\rm tot}\omega L^2})/\sqrt{\jmath\sigma^{-1}C_{\rm tot}\omega L^2}$. With $1/C_{\rm tot} = 1/C_{\rm ins} + 1/C_Q$, the measured quantum capacitance per unit area $C_Q = e^2\partial n/\partial\mu$ is a nonlocal compressibility, where n stands for the total TI charge and μ the value of the chemical potential at the TI surface. When two fluids are in mutual equilibrium, e.g., Dirac and/or VPSs with bulk states (BSs), they share the same surface chemical potential and their respective densities simply add in the total compressibility. The large thickness of our HgTe-TI samples allows us to model them as semi-infinite, and the compressibility is the sum of the upper surface and a semi-infinite bulk contribution. In the doped sample S_B, the sheet conductance includes a frequency-independent BS contribution.

Typical complex admittance spectra of S_A are shown in Figs. 2(a)–2(c) for $V_g = 0$ (Dirac point) and $V_g = 0.5$, 3 V (electron-doped regime). We observe three frequency domains: a quasistationary domain $Y/W = \jmath C_{\rm tot}L\omega + (C_{\rm tot}L\omega)^2\sigma^{-1}L/3$ (green shading), an intermediate domain (unshaded), and, finally, the evanescent wave domain (gray shading), where $\mathrm{Re}(Y) \simeq \mathrm{Im}(Y) \simeq W\sqrt{C_{\rm tot}\omega\sigma/2}$. The agreement between the experimental spectra and the distributed resistance-capacitance (RC) line model [solid lines in Figs. 2(a)–2(c)] is excellent and warrants the accuracy of the rf MITI-cap approach of compressibility. The RC line model allows extraction of a reliable value of the frequency-independent total capacitance $C_{\rm tot}$, insulator capacitance $C_{\rm ins} = C_{\rm tot}(V_g \to -\infty)$, quantum capacitance $C_Q(\mu) = C_{\rm ins}C_{\rm tot}/(C_{\rm ins} - C_{\rm tot})$, and conductivity $\sigma(V_g)$. Accounting for the nonlinear charge voltage characteristic, we calculate the total electron density $n = \frac{1}{e}\int C_{\rm tot}(V_g)dV_g$, the applied electric field $\mathcal{E}_{\rm ins} = ne/(C_{\rm ins}t_{\rm ins})$, and the surface chemical potential, $\mu(V_g) = e\int C_{\rm tot}/C_Q dV_g$. This allows one to plot $C_Q(\mu)$ and $\sigma(\mu)$ in Fig. 2(d) as well as the diffusion constant $\mathcal{D}(\mu) = \sigma/C_Q$ used for scattering spectroscopy in Fig. 2(e).

A similar chip with the same HgTe/CdHgTe heterostructure is produced, hosting $600 \times 200\ \mu$m Hall-bar structures, with the same optical lithography wet-etching technique equipped with a gold electrode as the gate on top of a 10-nm-thick HfO_2 insulator. Standard low-frequency ac techniques in a four-point measurement configuration are used at a temperature of 2 K in magnetic fields up to 2 T to measure the magnetic field and gate voltage V_g-dependent longitudinal sheet resistance R_{xx} and Hall resistance R_{xy}. The carrier density n can be accessed in the classical Drude transport regime by the magnetic field dependence of the Hall resistance. Two samples of types A and B analog to the MITI-cap samples with and without capping layer (not shown) were measured.

III. EXPERIMENT

Let us first give an overview of the compressibility measurements in samples S_A and S_B. As shown in the 10 kHz lock-in measurements of Fig. 3, a striking feature is the existence of a fully reversible compressibility in Fig. 3(a) [and a quasireversible one in Fig. 3(b)] below a maximum gate voltage $V_g^m = 3$ V. The absence of metastability warrants the absence of a bulk contribution, consistent with the magnetotransport measurements of Ref. [7]. In contrast, we observe above $V_g^m = 3$ V a prominent charge metastability up to the maximum amplitude, $V_g^m \gtrsim 10$ V, sustainable by the insulating dielectric stack. Metastability signals the onset of a second type of carrier and characterizes the breakdown of

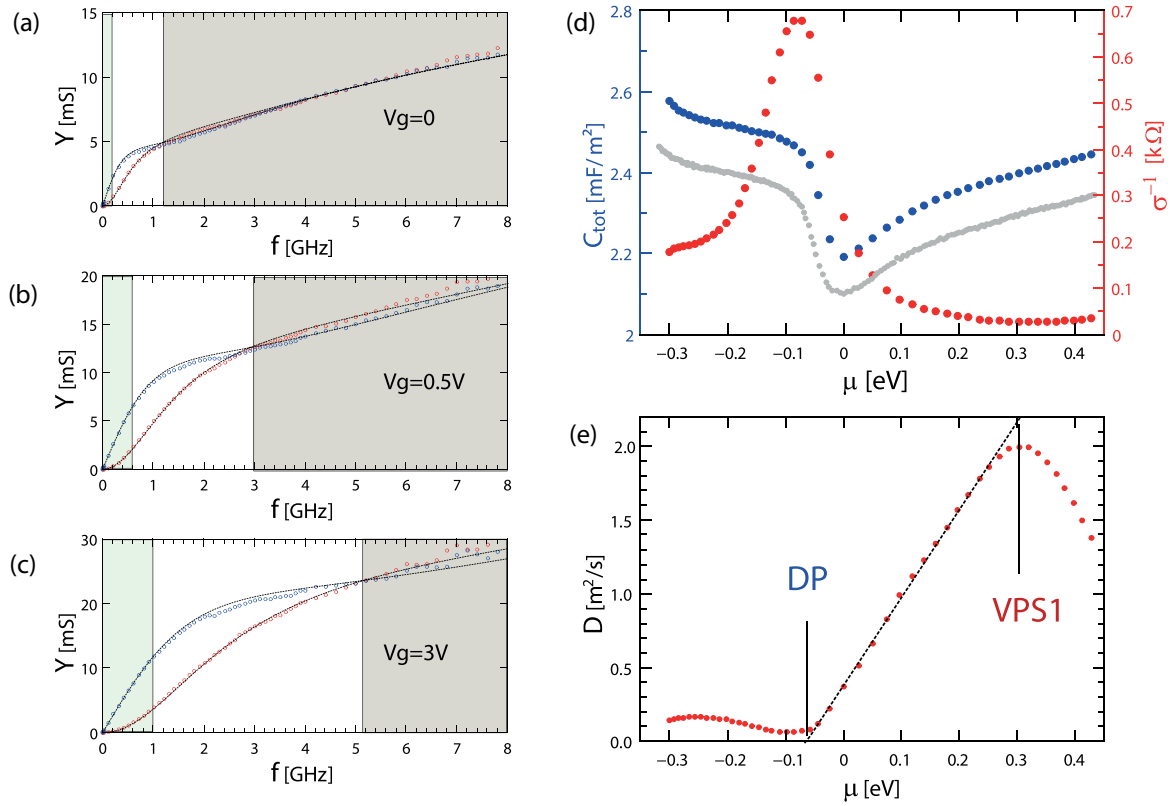

FIG. 2. Scattering spectroscopy evidence of a Volkov-Pankratov state in a HgTe/CdHgTe topological heterojunction. The quantum capacitance, conductivity, and diffusion constant are deduced from capacitor rf admittance measurements. (a)–(c) Broadband spectrum of the S_A-capacitor complex admittance $Y(f)$ [Re(Y) in red and Im(Y) in blue] for three typical gate voltages. The green shaded area corresponds to the quasistationary regime, $Y/W = \jmath C_{\rm tot} L\omega + (C_{\rm tot} L\omega)^2 \sigma^{-1} L/3$, where $C_{\rm tot}$ and σ^{-1} are the capacitance per unit area and the HgTe sheet resistivity. The gray shaded area is the evanescent wave regime where $\mathrm{Re}(Y) \simeq \mathrm{Im}(Y) \simeq W\sqrt{C_{\rm tot}\omega\sigma/2}$. (d) The quantum capacitance C_Q (blue dots), deduced by deembedding from $C_{\rm tot}$ the insulator capacitance $C_{\rm ins}$, and the sheet resistance σ^{-1} (red dots), deduced from fits of the ac-admittance spectra [solid lines in (a)–(c)], are plotted as a function of the chemical potential, as explained in the text. The dc measurement from Fig. 3(a) (gray dots) is added for comparison. The resistance shows an asymmetric peak close to neutrality. (e) The diffusion constant $\mathcal{D}(\mu) = \sigma/C_Q$ shows a dip at the Dirac point (DP), a linear increase in the electron regime corresponding to a Dirac-fermion-like high-mobility $\mu_e = 2e\mathcal{D}/\mu \simeq 12\ \mathrm{m^2\,V^{-1}\,s^{-1}}$, and a peak at $\Delta\mu \approx 0.35$ eV from the Dirac dip signaling the onset of a new and efficient scattering channel. We associate the maximum to the energy of the first Volkov-Pankratov state. Indeed the energy $\Delta\mu$ is very close to the theoretical prediction $E_{VP1} \approx 0.4$ eV.

Dirac screening. The hysteresis loops have a butterfly shape and a trend toward saturation at large negative V_g. We use this asymptotic value [horizontal lines in Figs. 3(a) and 3(b)] to estimate the insulator capacitance $C_{\rm ins}$. Note that the reversible curves are eventually history dependent themselves, with the displayed ones corresponding to the first charging cycles after cool down to $T = 10$ K. Reversible cycles subsequent to a high-field sweep are qualitatively similar but with a dip that is shifted in gate voltage and amplitude signaling the existence of trapped bulk carriers. We have checked that the MOM capacitance is linear and reversible in the same conditions, confirming that hysteresis is indeed associated to metastability in HgTe charging.

A. Compressibility of Dirac surface states

In both samples, the reversible charge response shows a capacitance dip attributed to the Dirac surface states near charge neutrality. In sample S_A, the dip is sharp and located at $V_g = 0$ V as expected for an intrinsic TI response. In sample S_B, the dip is shifted to $V_g = -1.2$ V, corresponding to an n-type doping density $n_0 = -2.6\ 10^{12}\ \mathrm{cm^{-2}}$ (bulk donor density $N_D = 4\ 10^{17}\ \mathrm{cm^{-3}}$), and smeared by this bulk carrier contribution. On subtracting the insulator contribution $1/C_{\rm ins}$ and integrating the relevant quantities, we deduce the surface chemical potential μ in the reversible state, which is plotted in Fig. 3(d) (sample S_A) as a function of $\mathcal{E}_{\rm ins}$. The S-shaped curve represents the charging path of the MITI-cap in the $\mu(\mathcal{E}_{\rm ins})$ representation. Similar curves are obtained for sample S_B (not shown). Finally, Fig. 3(c) shows the reversible $C_Q(\mu)$ plots of S_A (blue line) and S_B (green line). As expected from the additivity of compressibilities in a two-fluid system, one has $C_Q^B > C_Q^A$. In order to quantify the effect of bulk carriers, we have added in the figure the theoretical expectation (green dashed line) for the additional contribution of a trivial semiconductor to quantum capacitance with the above-estimated dopant density N_D. From the good experimental agreement, we conclude that the reversible $C_Q(\mu)$ plot of sample S_A is a close estimate of the intrinsic TI response. The linear energy dependence precludes an interpretation of compressibility in

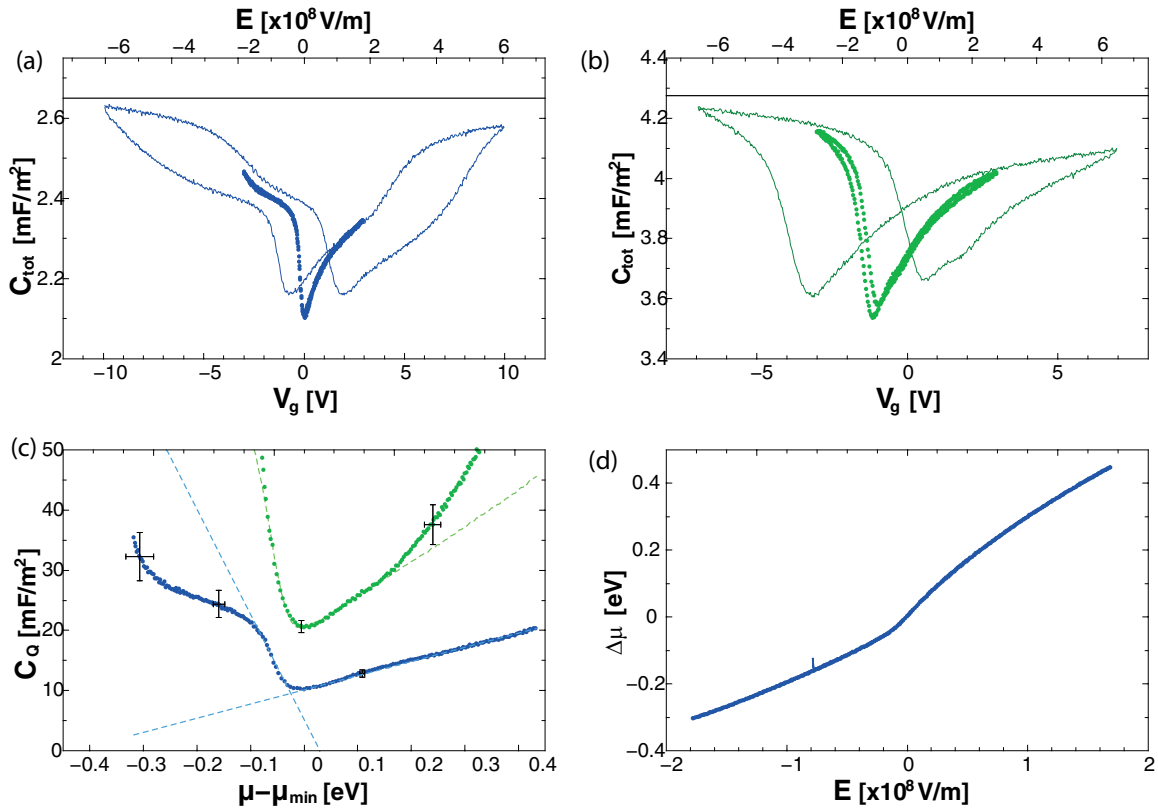

FIG. 3. Reversible surface-state compressibility and the breakdown of Dirac screening. Gate-voltage dependence of the capacitance in (a) the undoped capped sample S_A and (b) the uncapped doped sample S_B measured by lock-in techniques at 10 kHz. In both cases, we distinguish a low electric-field regime (bold lines) where $C_{\rm tot}(V_g)$ is reversible and a high-field regime ($V_g > 3V$) where MITI-cap charging is hysteretic. Both samples show a capacitance dip in the reversible regime corresponding to the Dirac point of the upper surface state. It is shifted in sample S_B, indicating an electron-type chemical doping of density $n \simeq 2.6\ 10^{12}$ cm^{-2}. From the capacitance saturation at large gate voltage, we deduce the insulator capacitance $C^A_{\rm ins} \simeq 2.65$ mF/m^2 and $C^B_{\rm ins} \simeq 4.27$ mF/m^2. (c) The surface chemical potential as a function of the applied electric field. (d) The quantum capacitance for samples S_A and S_B. The error bars are calculated taking a 1% uncertainty in the determination of the insulator capacitance. The main feature is the linear $C_Q(\mu)$ of sample S_A in the electron regime, which is a direct signature of the intrinsic TI compressibility. It extends over a broad range of electrostatic doping, ~ 0.3 eV. Details of the analysis of $C_Q(\mu)$ are given in the main text.

terms of conventional massive surface states. In fact, its energy dependence can be mapped to a Dirac fermion density of states, $C_Q = e^2\mu/(2\pi\hbar^2 v_F^2)$, with $v_F = 1.6\ 10^6$ ms^{-1} in the electron regime and $v_F = 0.5\ 10^6$ ms^{-1} in the hole regime. These values are larger than the accepted $v_F \simeq 1 \pm 0.2\ 10^6$ ms^{-1} [19]. Remarkably this Dirac-like response extends over a broad energy range ($\mu = -0.05 \rightarrow +0.30$ eV), widely exceeding the bulk transport band gap, consistent with the Dirac screening reported in Ref. [7]. In the data reduction, we have included a constant background $\sim$10 mF m^{-2} whose origin is not fully clarified. A possible explanation would be the nesting of the Dirac point in the heavy-hole Γ_8 branch, meaning that the observed compressibility minimum results from a superposition of a Dirac contribution with that of a heavy-hole Γ_8 band [42].

B. Scattering spectroscopy evidence of the first VPS

Here we focus on the sample S_A, which is the closest realization of an intrinsic CdHgTe/HgTe smooth THJ. Figure 2(d) shows $C_{\rm tot}(\mu)$ (blue dots) and $\sigma^{-1}(\mu)$ (red dots) deduced from admittance spectra in the reversible regime. The dc capacitance (gray dots) has been reproduced for comparison. The good agreement, besides a small amplitude shift due to calibration, shows that compressibility is frequency independent, confirming our analysis of admittance spectra that dissipative effects mainly stem from finite conductivity and not from an intrinsic $\chi(f)$ dependence. The resistivity exhibits a Dirac-like peak (DP) which is slightly shifted with respect to the capacitance dip, supporting our conjecture that the DP is nested in the Γ_8 band. The shape of the resistance reflects the electron-hole asymmetry of HgTe. The diffusion constant $\mathcal{D}(\mu) = \sigma/C_Q$ in Fig. 2(e) shows a minimum at $\mu \simeq -0.05$ eV and a linear increase in the electron regime up to $\mu \simeq 0.3$ eV, corresponding to a constant mobility $\mu_e = 2e\mathcal{D}/\mu \simeq 12$ m^2 V^{-1} s^{-1}. This large value is characteristic of massless Dirac fermions and is comparable with values deduced from magnetotransport experiments [7]. The diffusion constant $\mathcal{D}(\mu)$ is a marker of the scattering mechanism; its linear dependence is indicative of a screened charge disorder [34,35]. The most remarkable feature is a drop of $\mathcal{D}(\mu)$ at $\mu \simeq 0.3$ eV. We attribute this *scattering peak* to the onset of a new scattering channel for Dirac fermions when the surface Fermi energy $E_1 = \mu - E_{DP} \simeq 0.35$ eV crosses the bottom of a massive subband [23].

Since sample S_A is intrinsic, we can rule out the possibility that the scattering peak corresponds to a doping-induced

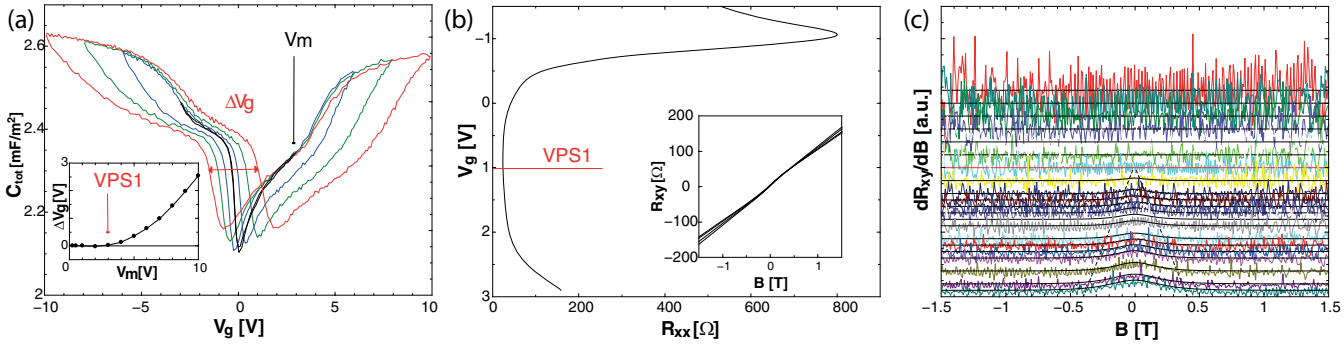

FIG. 4. Additional evidence of Dirac screening breakdown at high electric field. (a) Hysteresis loops of capacitance in sample S_A for increasing gate-voltage sweep amplitudes V_m (rainbow colors). As seen in the inset, the width ΔV of the hysteresis loops sets in at $V_g \geqslant 3$ V. It corresponds to the resistance minimum in Fig. 5(a) identified as the occurrence of the first VP state substantially and denoted as VP_1 above. Note also that the capacitance minima are shifted upward in the large V_g^m loops, indicating the presence of bulk carriers. (b) Longitudinal resistance R_{xx} and Hall resistance R_{xy} (inset) measured in a type-A Hall bar. A secondary resistance peak is observed in R_{xx}, similar to that in Fig. 5(a), which is accompanied by an S-shaped anomaly in $R_{xy}(B)$ (inset). The anomaly is highlighted in the $dR_{xy}/dB(V_g)$ waterfall plot in (c), where data are fitted by an empirical function $\alpha/\cosh^2(B/B_0)$ (solid lines). As the anomaly onset coincides with the resistance minimum (red line), we conclude that a second type of carrier does nucleate at the conductivity maximum denoted as VP_1.

massive surface state, as reported in [20,21]. The scattering peak energy $E_1 \simeq 0.35$ eV is very close to the theoretical estimate for the VPSs, $\Delta_1\sqrt{2(1+\Delta_2/\Delta_1)} \simeq 0.4$ eV. Identifying this energy with that of the first VPS band edge, $E_1 = \sqrt{2\hbar v_F(\Delta_1+\Delta_2)/\xi}$ [see Eq. (5) in the theory section IV], gives $\xi \simeq 6$ nm (with $v_F = 1.10^6$ m/s) close to the estimate $\xi \simeq 5$ nm deduced from numerical studies in Ref. [24]. From the agreement between theoretical and experimental determinations of the peak energy, we conclude that the scattering peak observed in Fig. 2(d) is a signature of the topological VPS subband [14,15] described in Sec. IV. A theoretical modeling of the peak shape, which would involve a detailed analysis of scattering and screening mechanisms in HgTe, remains beyond the scope of this work. Since C_Q is monotonic in the VPS1 energy range, the peak in $\mathcal{D}(\mu)$ translates into a peak in $\sigma(\mu)$. Figure 5(a) is an extension of Fig. 2(d) at the maximum gate-voltage span, taking the upward voltage sweep of the hysteresis loops. It shows that the conductance peak evolves into a resistance plateau at large electric field and that no additional conductance peak is observed in this sample.

C. Additional signatures of VPS carriers

VPSs, charge metastability, and Dirac screening breakdown. In Fig. 4, we analyze two complementary aspects of the TI charging phenomenology. Figure 4(a) shows a set of hysteretic charging characteristics $C_{\mathrm{tot}}(V_g)$ for increasing gate-voltage amplitudes V_g^m in sample S_A. They have a butterfly shape with two capacitance minima that are shifted upward or backward, depending on the direction of the voltage sweep. We attribute this metastability to the breakdown of Dirac screening and the nucleation of bulk carriers at high electric field, i.e., either electrons or holes, depending on the

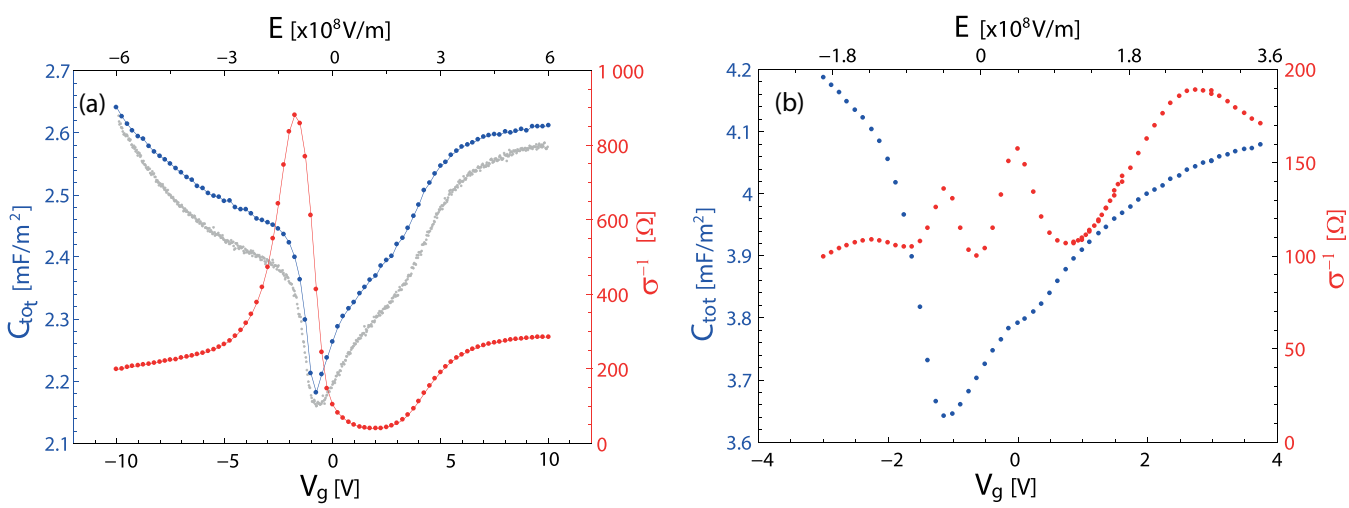

FIG. 5. High electric-field capacitance and resistivity measurements in samples (a) S_A and (b) S_B. The low-frequency data [gray dots in (a)] are added for comparison. To overcome hysteresis, the data are plotted for an increasing gate voltage. The most prominent features are the apparition of additional resistance peaks in the electron regime, with the Dirac peak being signaled by the capacitance dip. In sample S_A, the resistance peak is accompanied by a bump in the capacitance.

field history. The loop width $\Delta V_g(V_g^m)$ (inset of Fig. 4(a)) sets in at $V_g^m \simeq 3$ V and gradually increases up to $\Delta V_g \simeq 3$ V at $V_g^m \simeq 10$ V, corresponding to a bulk charge variation $\Delta n_B = \pm 2\ 10^{12}$ cm^{-2}. Note that the capacitance minima are shifted upward at large V_g^m, supporting the contribution of additional bulk carriers in the compressibility. The presence of charge metastability signals the Dirac screening breakdown.

Hall signature of VPS carriers. Figures 4(b) and 4(c) show the R_{xy}, R_{xx} magnetotransport measurements performed in a type-*A* Hall bar. The capped sample shows a clear maximum of the sheet resistance accompanied by a change in the sign of the Hall resistance (not shown), indicating the state with lowest carrier density at $V_g \approx -1.0$ V. Increasing the gate voltage (electron side) decreases the sheet resistivity σ^{-1} up to $V_g \approx 1.0$ V. For higher gate voltages, σ^{-1} increases monotonically with V_g [Fig. 4(c)] and a nonlinearity in the Hall resistance develops for low magnetic fields [inset of Fig. 4(b)]. The uncapped sample consistently shows additional peaks in the longitudinal resistance (not shown), with the only difference being that the *p*-conducting regime could not be reached in the available gate-voltage range due to the high (unintentional) *n* doping. Besides the Dirac peak (at $V_g = -1.1$ V), $R_{xx}(V_g)$ exhibits a secondary peak (at $V_g \simeq 3$ V) reminiscent of the one observed in the capacitor measurement of Fig. 5(a). The Hall resistance $R_{xy} \propto B$ develops an anomaly at $V_g \gtrsim 1$ V [inset of Fig. 4(b)], signaling the advent of a secondary carrier type. The anomaly is best depicted by plotting the derivative $\partial R_{xy}/\partial B$ in Fig. 4(c), where the base line is shifted according to the applied gate voltage. Data are fitted using an empirical function $\alpha/\cosh^2(B/B_0)$ (solid lines) used to extract the magnetic field range B_0 of the anomaly. We find $B_0 \propto (V_g - V_{g1})$ with $V_{g1} = 1.0$ V, corresponding to the resistance minimum in that sample. This shows that the scattering peak is indeed accompanied by the nucleation of a second carrier type, consistent with the VPS-subband interpretation. A similar analysis has been carried out in type-*B* samples, where we observe multiple R_{xx} peaks (not shown), also reminiscent of the capacitor measurement in Fig. 5(b).

D. The VPS phase diagram

The heuristic model below predicts a VP state series, $E_m = \sqrt{m}E_1$. In sample S_A, the second VPS, at $E_2 \simeq 0.5$ eV, is at the limit of experimental reach and deep in the metastable regime. This difficulty is circumvented in sample S_B, which has a finite *n*-type chemical doping and smaller E_m's due to a smaller capping band gap Δ_2 (see below). As shown in Fig. 5(b), the scattering spectroscopy is even richer: besides the Dirac peak identified by the capacitance dip, we observe *two resistance peaks* in the electron side and *one faint resistance peak* in the hole side. Similar to sample S_A [Fig. 5(a)], the conductance peaks (resistance dips) are not accompanied by capacitance features.

For direct comparison with theory, we provide in Fig. 6 a summary of our experimental observations. Figures 6(a) and 6(c) show the quantum capacitance and conductivity as a function of the TI charge density for both samples. We identify the Dirac peak position by the coinciding capacitance/conductance minima, and the VP states by the conductance maxima. These peaks are reported in the density–electric-field $n(\mathcal{E}_{\rm ins})$ diagrams of Figs. 6(b) and 6(d), which facilitates contact with more standard measurements where the surface chemical potential is not accessible experimentally. Note that $\mathcal{E}_{\rm ins}$ is the surface electric field at the insulator side, which differs from the HgTe-TI side by the ratio $\varepsilon_{\rm ins}/\varepsilon_{HgTe}$ of permittivities. The green lines in Figs. 6(b) and 6(d) are theoretical fits with the model below. As mentioned before, an advantage of this $n(\mathcal{E}_{\rm ins})$ diagram lies in the fact that the capacitor charging law reduces to a straight line. Actually, this is strictly true for the total TI charge, including bulk carriers. Later on, when comparing with theory, one should keep in mind that the theoretical phase diagram holds only for the surface-state density.

IV. THEORY

In this section, we describe the topological-normal junction giving rise to surface states over a penetration depth ξ within a simplified effective four-band model and a gradual interface of length ξ between the topological (inverted-gap) and the trivial (normal-gap) insulator. Besides the Dirac fermion, we find a set of degenerate massive surface states and we study the effect of an applied electric field on the surface-state spectra. Our theoretical modeling is corroborated with numerical $k \cdot P$ calculations of a gradual junction using six-band models particularly designed for HgTe.

A. Effective model of surface states

In order to model the insulating phases, we use the simplified linear four-band $k \cdot P$ Hamiltonian describing the bands around the Γ point of an inverted band structure [1],

$$\hat{H}_0(\mathbf{k},\Delta) = \begin{bmatrix} \Delta & \hbar v_F k_y & 0 & \hbar v_F(k_z - ik_x) \\ \hbar v_F k_y & -\Delta & \hbar v_F(k_z - ik_x) & 0 \\ 0 & \hbar v_F(k_z + ik_x) & \Delta & -\hbar v_F k_y \\ \hbar v_F(k_z + ik_x) & 0 & -\hbar v_F k_y & -\Delta \end{bmatrix}, \tag{1}$$

for which the spectrum consists of two doubly degenerate bands, $\varepsilon_k^{(\pm)} = \pm\sqrt{\Delta^2 + \hbar^2 v_F^2 k^2}$. This spectrum is independent of the sign of the gap parameter Δ. In the following, we model HgTe as an inverted insulator of gap $-\Delta_1 < 0$ that is in contact with a normal insulator of gap $\Delta_2 > 0$. The corresponding bulk Hamiltonians are $\hat{H}_0(\mathbf{k}, -\Delta_1)$ and $\hat{H}_0(\mathbf{k},\Delta_2)$ as represented on the left- and right-hand sides of Fig. 7(a).

We consider that HgTe is located in a region $z < 0$ and that the normal insulator (CdHgTe or HfO_2) is located at $z > \xi$. We model the interface $0 < z < \xi$ between the two

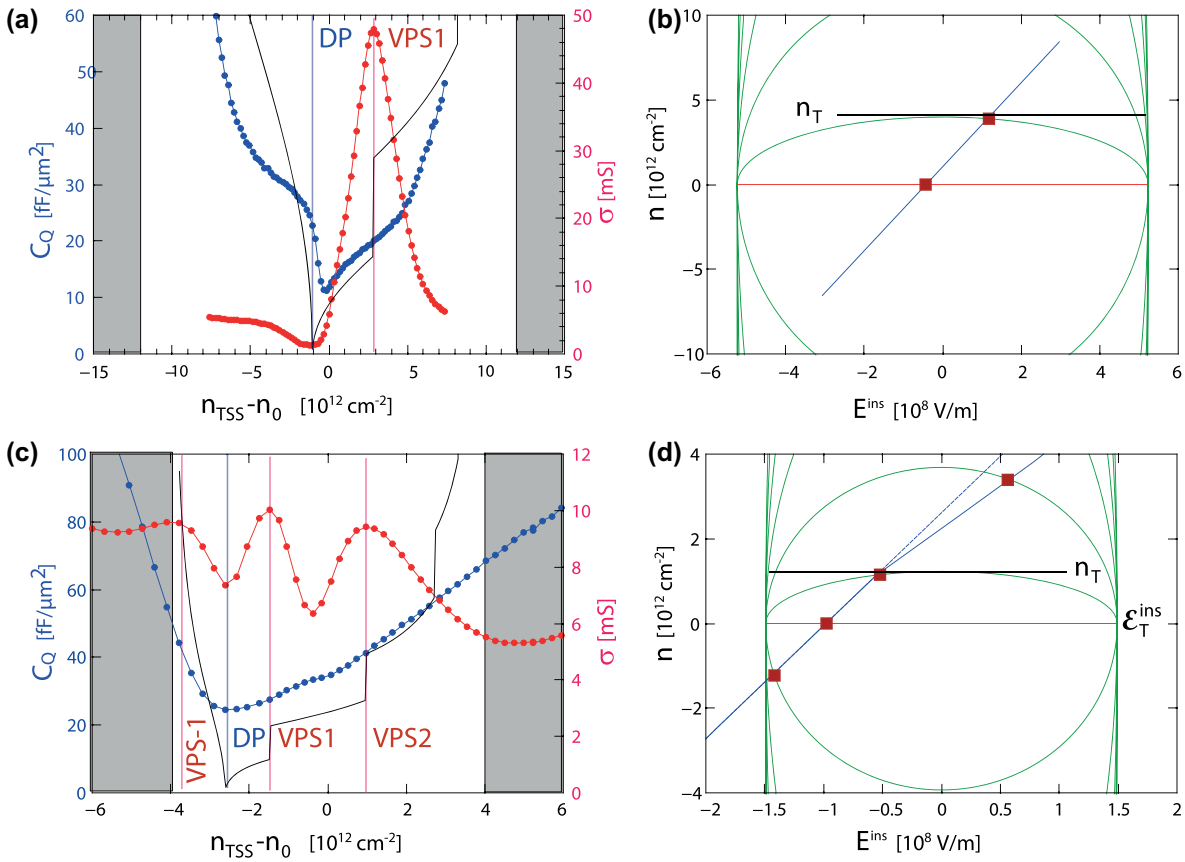

FIG. 6. Density–electric-field phase diagram of strained bulk HgTe. The compressibility-conductance data (blue-red data points) from samples (a) S_A and (c) S_B are compared to the prediction of the model in Sec. IV. By adjusting the resistance peak positions with respect to the Dirac point, we deduced the model parameters (see the text). (b),(d) The green solid lines correspond to the theoretical predictions of energies of the surface states. Square signals correspond to energies of VP states extracted from experiment. The MITI-cap charging paths are included in the n–$\mathcal{E}$ phase diagram as depicted in (b) and (d). These phase diagrams are obtained from the $\mathcal{E}$ behavior of the VP surface states (6) plotted in Fig. 7(b) (see theory section IV). From this analysis, we deduce the critical electric field of the THJ beyond which surface states completely disappear: $\mathcal{E}_T^A = 2.64\times10^8$ Vm^{-1} and $\mathcal{E}_T^B = 0.81\times10^8$ Vm^{-1}. The smaller $\mathcal{E}_T$ in S_B is due to the absence of a capping layer. Above $\mathcal{E}_T$, the topological-trivial insulator interface behaves as a normal, nontopological interface. Two such subbands can be seen in S_B due to chemical doping and a lower excitation gap.

semiconductors using an interpolating Hamiltonian $\hat{H}_{s0} = \hat{H}_0[\mathbf{k}, -\Delta_1 + e\mathcal{E}_T z]$ with the characteristic field

$$\mathcal{E}_T = \frac{\Delta_1 + \Delta_2}{e\xi}. \tag{2}$$

This field plays the role of a confinement or gap field that we have chosen to have the same physical dimension as an electric field. The evolution of the gap is sketched as a green line in Fig. 7(a) and can be viewed as a three-dimensional generalization of the procedure described in Ref. [13] for a one-dimensional system and in Ref. [37] for Weyl semimetals. The Hamiltonian contains a pair of noncommuting variables $[z,k_z] \neq 0$ that can be merged into the same matrix elements with the help of a k-independent unitary transformation $|\Psi\rangle = \hat{U}|\Psi'\rangle$. One finds, in this new basis,

$$\hat{H}'_{s0} = \hat{U}^\dagger \hat{H}_{s0} \hat{U} = \begin{bmatrix} \hbar v_F k_x & \hbar v_F k_y & 0 & \sqrt{2\hbar v_F e\mathcal{E}_T}\hat{a}^\dagger \\ \hbar v_F k_y & -\hbar v_F k_x & \sqrt{2\hbar v_F e\mathcal{E}_T}\hat{a}^\dagger & 0 \\ 0 & \sqrt{2\hbar v_F e\mathcal{E}_T}\hat{a} & \hbar v_F k_x & -\hbar v_F k_y \\ \sqrt{2\hbar v_F e\mathcal{E}_T}\hat{a} & 0 & -\hbar v_F k_y & -\hbar v_F k_x \end{bmatrix}, \tag{3}$$

where we have introduced the ladder operators $\hat{a} = [\hbar v_F k_z - i(e\mathcal{E}_T z - \Delta_1)]/\sqrt{2\hbar v_F e\mathcal{E}_T}$ and $\hat{a}^\dagger = [\hbar v_F k_z + i(e\mathcal{E}_T z - \Delta_1)]/\sqrt{2\hbar v_F e\mathcal{E}_T}$ such that $[\hat{a},\hat{a}^\dagger] = 1$. This Hamiltonian is similar to that in a magnetic field [38] and we introduce the number states $|m\rangle$ associated to the number operator $\hat{m} = \hat{a}^\dagger\hat{a}$, with $\hat{m}|m\rangle = m|m\rangle$. These states are localized at the interface between two insulators with a mean position $\langle z\rangle = \Delta_1/e\mathcal{E}_T = \Delta_1\xi/(\Delta_1 + \Delta_2) \in [0,\xi]$.

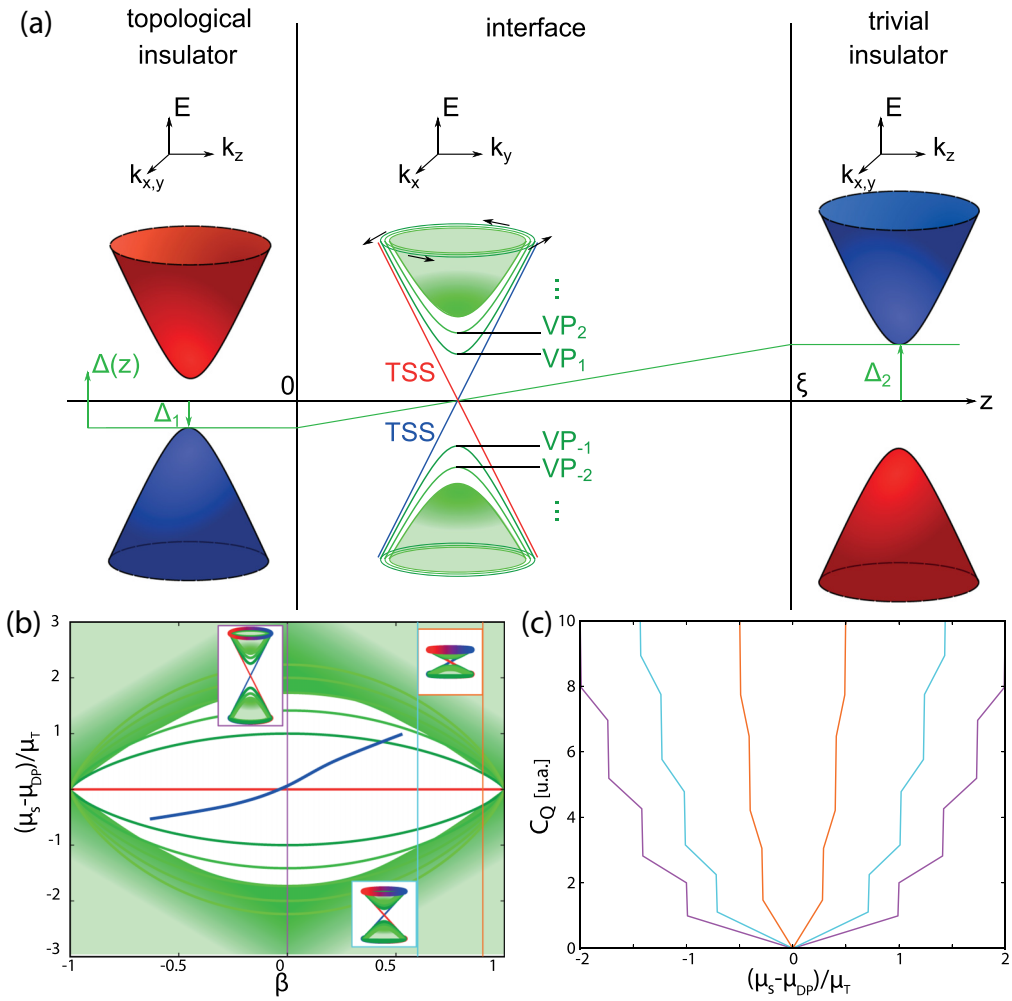

FIG. 7. Model of massive surface states (VPSs) in topological insulators. (a) Simplified model for the interface of a topological insulator (left) and a normal insulator (right). In the interface, one observes multiple surface states. (b) Band gaps of the Dirac and VP states as a function of the reduced electric field $\beta = \mathcal{E}/\mathcal{E}_T$. The blue solid line is a sketch of a capacitor charging line measured in Fig. 3(d). (b) Equivalent to the $n - \mathcal{E}$ phase diagram of Figs. 6(b) and 6(c). (c) Illustration of the double effect of electric field in the quantum capacitance $C_Q(\mu,\mathcal{E})$ for selected values of the parameters represented by colored lines in (b). The group velocity of the Dirac fermion decreases with increasing electric field and its density of states rises up to the critical field with a vanishing of the Fermi velocity $C_Q(\mu)_{\mathcal{E}\to\infty}$ at the critical field $\mathcal{E}_T$. At finite doping, the subbands cross the Fermi energy at $\mathcal{E} < \mathcal{E}_T$, giving rise to a stepwise increase of $C_Q(\mathcal{E})_{\mu=Cte}$.

For $m \geqslant 1$, one finds an infinite number of states of the form $|\Psi_{m,\mathbf{k}}\rangle = (\alpha_1|m\rangle,\alpha_2|m\rangle,\alpha_3|m-1\rangle,\alpha_4|m-1\rangle)$. Their band dispersion is doubled in that one finds, for each value of m, a band at positive and negative energy,

$$\varepsilon^{(\pm)}_{m,k_x,k_y} = \pm\sqrt{\hbar^2 v_F^2\left(k_x^2 + k_y^2\right) + 2\hbar v_F e\mathcal{E}_T m}, \tag{4}$$

which yields the relevant $\mathbf{k} = 0$ separation,

$$\begin{aligned} E_{\pm m} &= \varepsilon^{(\pm)}_{m,k_x=k_y=0} = \pm\sqrt{2\hbar v_F e\mathcal{E}_T m} \\ &= \pm\sqrt{2\hbar v_F(\Delta_1 + \Delta_2)m/\xi}, \end{aligned} \tag{5}$$

between the VPSs, as already mentioned in Sec. III B in the estimation of the surface width ξ. In addition, these states, which were first identified by Volkov and Pankratov in 1985 [14], are doubly degenerate and depend explicitly on the characteristic field (2) and thus on the parameters characterizing the interface. In the limit of a sharp surface, i.e., $\xi \to 0$ so that $\mathcal{E}_T \to \infty$, these states are shifted to high energies and do not play any physical role.

In contrast to these bands, the $m = 0$ surface states are not degenerate. They are of the form $|\Psi_{0,\mathbf{k}}\rangle = (\alpha_1|0\rangle,\alpha_2|0\rangle,0,0)$ and their energy dispersion is that of a two-dimensional Dirac cone, $\varepsilon^{(\pm)}_{0,k_x,k_y} = \pm\hbar v_F\sqrt{k_x^2 + k_y^2}$. It is independent of $\mathcal{E}_T$ and one can show [37] that this state is of a topological nature. This topological surface state survives in the limit of an infinitely sharp interface, as expected, and shows a dispersion that only depends on the bulk parameter v_F, in agreement with previous studies [1]. We represent the spectra of the VPS$_{\pm m}$ states and the Dirac state in Fig. 7(a).

Most saliently, the VPS can be modified to great extent by an electric field applied perpendicular to the interface. As an effect of charge screening, the associated electrostatic potential drops in the interface and generates an electric field $\boldsymbol{\mathcal{E}} \equiv -\mathcal{E}\mathbf{e}_z \approx -V_0/\xi\mathbf{e}_z$, where $V_0 = \mu/e$ is the surface potential. The interface Hamiltonian, for $0 < z < \xi$, is

now $\hat{H}_s = \hat{H}'_{s0} + (V_0 - e\mathcal{E}z)\mathbb{1}$. Notice that the added term remains invariant under the above-mentioned rotation that leads to the form of the Hamiltonian given by Eq. (3). As detailed in the Appendix, the spectrum now depends on the ratio $\beta = \mathcal{E}/\mathcal{E}_T$ between the applied and the characteristic electric fields. The spectrum for the $m \geqslant 1$ states is still doubly degenerate with the dispersion relations $\varepsilon_{m,k_x,k_y}(\beta) = \sqrt{(1-\beta^2)\hbar^2 v_F^2(k_x^2+k_y^2) + 2m(1-\beta^2)^{3/2}\hbar v_F e\mathcal{E}_T}$. One observes that the gap (5) is reduced by the applied electric field according to

$$E_{\pm m}(\mathcal{E}) = \pm\sqrt{m}\,\sqrt{2\hbar v_F e\mathcal{E}_T}\,\left(1-\mathcal{E}^2/\mathcal{E}_T^2\right)^{3/4}, \tag{6}$$

and that the critical surface density obeys

$$n_m(\mathcal{E}) = \frac{m(m+1)}{2}\,\frac{e\mathcal{E}_T}{2\pi\hbar v_F}\,\left(1-\mathcal{E}^2/\mathcal{E}_T^2\right)^{1/2}. \tag{7}$$

At the same time, the dispersion relation flattens out because of the reduced Fermi velocity that vanishes at $\mathcal{E}_T$ according to

$$v_F(\mathcal{E}) = v_F\,\left(1-\mathcal{E}^2/\mathcal{E}_T^2\right)^{1/2}. \tag{8}$$

The special $m = 0$ surface state is also flattened and one finds $\varepsilon^{(\pm)}_{0,k_x,k_y} = \pm(1-\beta^2)^{1/2}\hbar v_F\sqrt{k_x^2+k_y^2}$.

In Fig. 7(b), we represent the extrema of the VPS$_{\pm m}$ (in green) and of the Dirac state at $k_x = k_y = 0$ (in red) as a function of $\beta = \mathcal{E}/\mathcal{E}_T$. We observe that VPSs merge for an electric field close to the critical field $\mathcal{E}_T$. Beyond this limit, our model (A1) has no bound state so that the interface behaves as a conventional semiconducting heterojunction. This shows that $\mathcal{E}_T$ is not only a characteristic field governing the massive surface-state spectrum, but is actually a genuine critical field for the topological nature of the interface. The applied electric potential also influences the chemical potential (blue line in Fig. 7) that will eventually cross the VPSs. This leads to kinks in the compressibility and features in the conductivity that we discuss in detail in the following section.

We finish this theoretical section with a discussion of the density of states $\rho(\epsilon)$, which is directly proportional to the quantum capacitance (at $T = 0$). The density of states associated with the surface states per unit area reads

$$\rho(\varepsilon) = \frac{|\varepsilon|}{2\pi\hbar^2 v_F^2(1-\beta^2)}\sum_l \Theta[|\varepsilon| - (1-\beta^2)^{3/4}\sqrt{2\hbar v_F e\mathcal{E}_T m}], \tag{9}$$

where $\Theta(x)$ is the Heaviside function. The corresponding behavior of the quantum capacitance is represented in Fig. 7(c) for typical values of $\beta = \mathcal{E}/\mathcal{E}_T$. One observes that the gaps are smaller and that the density of states becomes enhanced for larger electric fields (in red). This is a direct consequence of the reduced Fermi velocity in the presence of an electric field, as pointed out above. Notice, however, that in the experimental setup, the chemical potential depends on the applied electric potential and therefore jumps from one curve to the other. Moreover, we expect this density of state to be smeared in the presence of disorder.

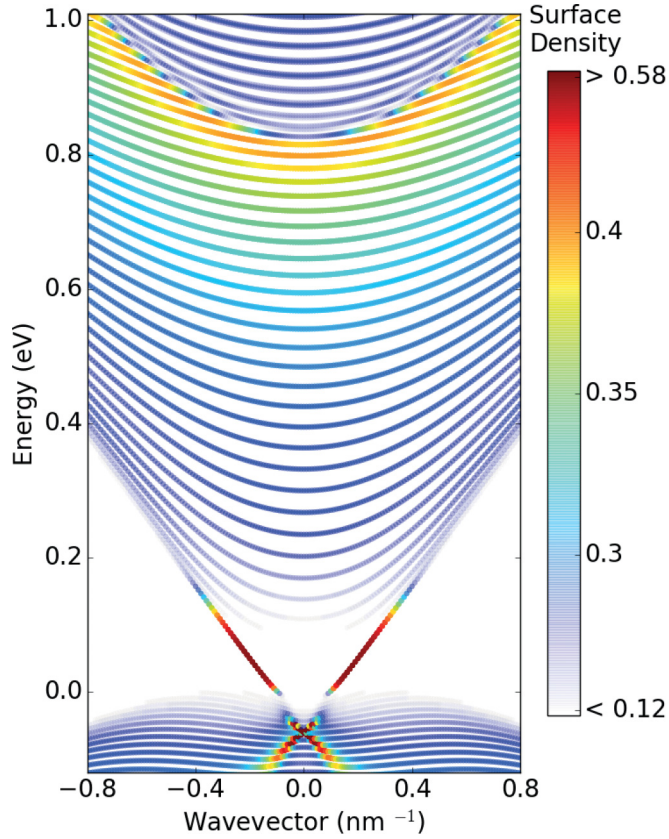

FIG. 8. Numerical dispersion relation $E(k_\parallel)$ for an HgTe/CdTe interface obtained within a six-band Kane model. $k_\parallel$ corresponds to the momentum along the interface. The color encodes the density of eigenstates in a region of ∼6 nm around the interface. The existence of localized states around the interface is shown within the gap but also at high energy around 1 eV.

B. Numerical $k \cdot P$ treatment of surface states

To complement the previous analytical study, we have performed a numerical study of the band structure of an HgTe/CdTe interface, based on a $k \cdot P$ model. Our numerical approach amounts to discretizing a standard Kane model for the six-band $\Gamma_{6,\pm1/2}, \Gamma_{8,\pm1/2}, \Gamma_{8,\pm3/2}$ Hamiltonian with parameters for HgTe and CdTe known from the literature [39]. The parameters of the model are interpolated between their values in both materials over a distance ξ corresponding to the size of the interface. This description incorporates the stress induced by the lattice mismatch through a Bir-Pikus term. The resulting band structure is shown in Fig. 8, where the color encodes the eigenstate's density around the HgTe/CdTe interface. The band structure is calculated for an HgTe thickness of 70 nm and $\xi = 5$ nm. Note that this band structure is obtained at zero electric field and using CdTe ($2\Delta_2 \simeq 1.5$ eV) as a capping layer boundary. We find a massive surface subband at 1 eV, which is accompanied by a strong depletion of the bulk state amplitude in the surface layer that confirms the above picture of high-energy surface states (VPSs). The excitation energy is quite large (still smaller than $2\Delta_2$) and found to be sensitive to the detail of the shape of the smooth interface. This is consistent with the analytical approach of Sec. IV A, which focuses on a linear interpolation

between the two materials and neglects asymmetry between the two materials beyond the gap inversion. We stress that these VPSs are predicted at zero electric field and assume that they follow the electric-field dependence predicted by the approach of Sec. IV A, as corroborated by Ref. [15].

V. COMPARISON WITH EXPERIMENT

The main evidence of VPSs is the scattering peak observed in the intrinsic sample S_A [Figs. 2(e) and 6(a)], where the absence of the classical massive surface state and the Dirac screening of bulk states have been previously warranted experimentally [7]. The measured VPS1 gap $E_1 = 0.35$ eV is close to the theoretical value $E_1(0) \simeq 0.4$ eV, deduced from Eq. (6), and is accompanied by a second carrier type observed in the Hall-bar measurements. In addition, we report that the VPS1 triggers the onset of charge metastability, signaling the breakdown of Dirac screening [7].

The second evidence is the observation of a series of scattering peaks in the uncapped sample S_B [Figs. 5(b) and 6(c)]. Since the capping of sample S_B is ill defined, we cannot make a direct comparison of VPS energy with theory so that Δ_2 becomes a fitting parameter. Still, we can adjust the peaks series with the predicted sequence $n_m \propto m(m+1)/2$ of Eq. (7).

The third evidence relates to the electric-field redshift. As seen in Fig. 6(d), the agreement of VPS spectroscopy with theory involves a ~10% electric-field redshift for the VPS2 state of sample S_B, consistent with Eq. (6). As for the VPS-1 state, its observation fully relies on a strong-field renormalization of the gaps, meaning that the VPS-1 peak position signals the vicinity of the critical field $\mathcal{E}_T$. The fact that VPS-1 is smeared is also consistent with theory since the Fermi velocity vanishes at $\mathcal{E}_T$ according to Eq. (8). Moreover, the conductivity becomes featureless above $\mathcal{E}_T$, also in agreement with theory. Our scattering spectroscopy measurements thus support the field-effect-induced redshift and suppression of VPS predicted in Sec. IV. Although a deeper insight into the field suppression is desirable, it remains very challenging as a full mapping of the $n(\mathcal{E})$ diagram would require an *in situ* tuning of the insulator permittivity and/or TI chemical doping. An extension of this work can be envisioned using a series of similar HgTe THJs with varied capping band gap Δ_2 and/or insulator permittivity $\varepsilon_{\rm ins}$.

Before concluding, let us detail our analysis of the $n(\mathcal{E})$ phase diagrams in Figs. 6(b) and 6(d). Equation (7) predicts subband minima for a surface-state density $n_m = n_1 \times \frac{m(m+1)}{2}\sqrt{1-\beta^2}$, where $n_1 = e\mathcal{E}_T/2\pi\hbar v_F$ and $\beta = \mathcal{E}_{HgTe}/\mathcal{E}_T = \varepsilon_{\rm ins}\mathcal{E}_{\rm ins}/\varepsilon_{HgTe}\mathcal{E}_T$. Taking $\mathcal{E}_T = 1.2\ 10^8$ V/m, $\varepsilon^A_{\rm ins} = C_{\rm ins}t_{\rm ins}/\varepsilon_0 \simeq 4.5$, and $\varepsilon_{HgTe} \simeq 20$ [29,30], we estimate for sample S_A the applied critical field $\mathcal{E}^A_c = \varepsilon_{HgTe}\mathcal{E}_T/\varepsilon^A_{\rm ins} \simeq 5\ 10^8$ Vm^{-1}, and a surface critical density $n^A_1 = 2.9\ 10^{12}$ cm^{-2} (with $v_F = 10^6$ m/s). The direct total charge measurement gives a larger $n_1 \simeq 4\ 10^{12}$ cm^{-2} due to the presence of bulk carriers. The same analysis can be carried out for the doped sample S_B, where we obtain a quantitative agreement for the position of three VPS peaks (VPS-1, VPS2, and VPS3) with a single parameter $\mathcal{E}^B_T = (0.4 \pm 0.1)\ 10^8$ Vm^{-1}, yielding $n^B_1 = 1\times10^{12}$ cm^{-2}. The fact that $\mathcal{E}^B_T \simeq \mathcal{E}^A_T/3$ highlights the importance of a capping layer in strengthening the robustness of surface topological states.

Finally, we have plotted in Figs. 6(a) and 6(c) (solid black lines) the theoretical prediction for the quantum capacitance calculated from the density of states of surface states in Eq. (9). While we see the linear increase of a secondary carrier density in the Hall-bar measurements, we do not resolve the compressibility steps signaling the onset of massive subbands. A possible reason for this discrepancy is the presence of residual bulk carriers, obscuring the compressibility resolution and explaining the compressibility background observed in Fig. 3(d). These carriers can be disorder-induced small-scale charge puddles or, more likely, in our high-mobility samples, large-scale puddles induced by the nonuniformity of the applied electrostatic surface potential. Considering the small transport band gap of HgTe, the potential uniformity requirements are especially stringent.

VI. CONCLUSION

Our comprehensive set of measurements, complemented by a heuristic model, supports the existence of intrinsic massive surface states, the Volkov-Pankratov states, and accompanying Dirac states at the interface between TI HgTe and the insulator CdHgTe. Such high-energy topological states, which are intrinsic to topological matter, have long been predicted [13,14]. Our work is a report and systematic study of these states, and we hope it will trigger further investigations into different materials such as the Bi-based TI [40] or different topological phases such as massive Majorana states, helical edge states, or Fermi arcs. As pointed out in Ref. [13] and demonstrated in this experiment, massive surface states play an important role in restricting the phase diagram where topological protection is robust, such as the Dirac screening [13] which is explained here as a relativistic field effect. This phase diagram can be enriched by applying an external magnetic field or simply by increasing the temperature, highlighting the possible role of electron-electron interactions.

ACKNOWLEDGMENTS

We gratefully acknowledge B.A. Bernevig, N. Regnault, R. Ferreira, Y. Guldner, G. Bastard, and M. Civelli for fruitful discussions. B.A.A. acknowledges funding from ANR-LabEx grant ENS-ICFP ANR-10-LABX-0010/ANR-10IDEX-0001-02PSL. We acknowledge financial support from the German Research Foundation DFG (the Leibniz Program, Sonderforschungsbereich 1170 Tocotronics and Schwerpunktprogramm 1666), the EU ERC-AG program (Projects 3-TOP and 4 TOPS), the Elitenetzwerk Bayern IDK Topologische Isolatoren and the Helmoltz Foundation (VITI).

APPENDIX: LORENTZ BOOST OF SURFACE STATES IN AN ELECTRIC FIELD

In Sec. IV A, we have introduced the Hamiltonian $\hat{H}_s = \hat{H}'_{s0} + (V_0 - e\mathcal{E}z)\mathbb{1}$. In order to deal with this z dependence, we perform a Lorentz boost on the time-independent Schrödinger equation $e^{\frac{\eta}{2}\hat{J}}(\hat{H}'_s - \varepsilon\mathbb{1})e^{\frac{\eta}{2}\hat{J}}|\bar{\Psi}\rangle = 0$, where the Lorentz boost [41] is realized by the hyperbolic transformation $|\Psi'\rangle = \mathcal{N}e^{-\frac{\eta}{2}\hat{J}}|\Psi\rangle$ generated by $\hat{J} = \sigma_y \otimes \sigma_x$, in terms of the Pauli matrices σ_x and σ_y.

In the case $\tanh(\eta) \equiv \beta = \mathcal{E}/\mathcal{E}_T \in [-1,1]$ and $V_0 = -\beta\Delta_1$, one can thus make the $(V_0 - e\mathcal{E}z)\mathbb{1}$ term vanish in the comoving frame of reference. If we define the pseudomagnetic field $B = \mathcal{E}_T/v_F$, this transformation can be understood from the viewpoint of *special relativity* as a boost to a frame of reference where the drift velocity $v_D = \mathcal{E}/B$ vanishes [41]. The condition $\mathcal{E}/\mathcal{E}_T = v_D/v_F \in [-1,1]$ is similar to the existence of a limiting velocity; the Fermi velocity v_F plays the role of the speed of light in special relativity. The Schrödinger equation becomes $\hat{H}_s'|\bar{\Psi}\rangle = \varepsilon|\bar{\Psi}\rangle$ with

$$\hat{H}_s' = \begin{bmatrix} \hbar v_F' k_x & \hbar v_F' k_y & 0 & \sqrt{2\hbar v_F' e\mathcal{E}_T'}\hat{b} \\ \hbar v_F' k_y & -\hbar v_F' k_x & \sqrt{2\hbar v_F' e\mathcal{E}_T'}\hat{b} & 0 \\ 0 & \sqrt{2\hbar v_F' e\mathcal{E}_T'}\hat{b}^\dagger & \hbar v_F' k_x & -\hbar v_F' k_y \\ \sqrt{2\hbar v_F' e\mathcal{E}_T'}\hat{b}^\dagger & 0 & -\hbar v_F' k_y & -\hbar v_F' k_x \end{bmatrix}, \tag{A1}$$

with $v_F' = \sqrt{1-\beta^2}v_F$, $\mathcal{E}_T' = (1-\beta^2)\mathcal{E}_T$, and the ladder operators $\hat{b},\hat{b}^\dagger$, where

$$\hat{b} = \frac{1}{(1-\beta^2)^{1/4}\sqrt{2\hbar v_F' e\mathcal{E}_T'}}\left\{\hbar v_F k_x - i\sqrt{1-\beta^2}\left[e\mathcal{E}_T z - \left(\Delta_1 + \frac{\beta}{\beta^2-1}\varepsilon\right)\right]\right\}, \tag{A2}$$

$$\hat{b}^\dagger = \frac{1}{(1-\beta^2)^{1/4}\sqrt{2\hbar v_F' e\mathcal{E}_T'}}\left\{\hbar v_F k_x + i\sqrt{1-\beta^2}\left[e\mathcal{E}_T z - \left(\Delta_1 + \frac{\beta}{\beta^2-1}\varepsilon\right)\right]\right\}. \tag{A3}$$

As a consequence of the Lorentz boost, the ladder operators are now explicitly energy dependent as well as the mean position of the number states $\langle z\rangle = (\Delta_1 + \frac{\beta}{\beta^2-1}\varepsilon)/e\mathcal{E}_T$. For our theory to describe a surface state, this position must be within $\langle z\rangle \in [0,\xi]$, and one notices that for $\beta \to 1$, this condition is not fulfilled for $\varepsilon \neq 0$.

The spectrum is found using states of the form $|\Psi_{m,\mathbf{k}}\rangle = (\alpha_1|m\rangle,\alpha_2|l\rangle,\alpha_3|m-1\rangle,\alpha_4|m-1\rangle)$ for $m \geqslant 1$ and $|\Psi_{0,\mathbf{k}}\rangle = (\alpha_1|0\rangle,\alpha_2|0\rangle,0,0)$ for $m = 0$, in the comoving frame of reference. The $|m\rangle$ states are the eigenstates of the number operator $\hat{m} = \hat{b}^\dagger\hat{b}$.

[1] X.-L. Qi and S.-C. Zhang, Topological insulators and superconductors, Rev. Mod. Phys. **83**, 1057 (2011).

[2] B. A. Bernevig, T. L. Hughes, and S.-C. Zhang, Quantum spin Hall effect and topological phase transition in HgTe quantum wells, Science **314**, 1757 (2006).

[3] L. Fu, C. L. Kane, and E. J. Mele, Topological Insulators in Three Dimensions, Phys. Rev. Lett. **98**, 106803 (2007).

[4] P. Hosur and X. Qi, Recent developments in transport phenomena in Weyl semimetals, C. R. Phys. **14**, 857 (2013).

[5] S. Y. Xu, I. Belopolski, N. Alidoust, M. Neupane, G. Bian, C. L. Zhang, R. Sankar, G. Q. Chang, Z. J. Yuan, C. C. Lee, S. M. Huang, H. Zheng, J. Ma, D. S. Sanchez, B. K. Wang, A. Bansil, F. C. Chou, P. P. Shibayev, H. Lin, S. Jia, and M. Z. Hasan, Discovery of a Weyl fermion semimetal and topological Fermi arcs, Science **349**, 613 (2015).

[6] M. Konig, S. Wiedmann, C. Brune, A. Roth, H. Buhmann, L. W. Molenkamp, X. L. Qi, and S. C. Zhang, Quantum spin Hall insulator state in HgTe quantum wells, Science **318**, 766 (2007).

[7] C. Brüne, C. Thienel, M. Stuiber, J. Böttcher, H. Buhmann, E. G. Novik, C.-X. Liu, E. M. Hankiewicz, and L. W. Molenkamp, Dirac-Screening Stabilized Surface-State Transport in a Topological Insulator, Phys. Rev. X **4**, 041045 (2014).

[8] J. Wiedenmann, E. Bocquillon, R. S. Deacon, S. Hartinger, O. Herrmann, T. M. Klapwijk, L. Maier, C. Ames, C. Brune, C. Gould, A. Oiwa, K. Ishibashi, S. Tarucha, H. Buhmann, and L. W. Molenkamp, 4 pi-periodic Josephson supercurrent in HgTe-based topological Josephson junctions, Nat. Commun. **7**, 10303 (2016).

[9] E. Bocquillon, R. S. Deacon, J. Wiedenmann, P. Leubner, T. M. Klapwijk, C. Brüne, K. Ishibashi, H. Buhmann, and L. W. Molenkamp, Gapless Andreev bound states in the quantum spin Hall insulator HgTe, Nat. Nanotechnol. **12**, 137 (2017).

[10] R. S. Deacon, J. Wiedenmann, E. Bocquillon, F. Domínguez, T. M. Klapwijk, P. Leubner, C. Brüne, E. M. Hankiewicz, S. Tarucha, K. Ishibashi, H. Buhmann, and L. W. Molenkamp, Josephson Radiation from Gapless Andreev Bound States in HgTe-Based Topological Junctions, Phys. Rev. X **7**, 021011 (2017).

[11] L. Wu, M. Salehi, N. Koirala, J. Moon, S. Oh, and N. P. Armitage, Quantized Faraday and Kerr rotation and axion electrodynamics of the surface states of three-dimensional topological insulators, Science **354**, 1124 (2016).

[12] V. Dziom, A. Shuvaev, A. Pimenov, G. V. Astakhov, C. Ames, K. Bendias, J. Böttcher, G. Tkachov, E. M. Hankiewicz, C. Brüne, H. Buhmann, and L. W. Molenkamp, Observation of the universal magnetoelectric effect in a 3D topological insulator, Nat. Commun. **8**, 15197 (2017).

[13] T. Karzig, G. Refael, and F. von Oppen, Boosting Majorana Zero Modes, Phys. Rev. X **3**, 041017 (2013).

[14] B. A. Volkov and O. A. Pankratov, Two-dimensional massless electrons in an inverted contact, JETP Lett. **42**, 178 (1985).

[15] S. Tchoumakov, V. Jouffrey, A. Inhofer, E. Bocquillon, B. Plaçais, D. Carpentier, and M. O. Goerbig, Volkov-Pankratov states in topological heterojunctions, Phys. Rev. B **96**, 201302(R) (2017).

[16] D. Hsieh, D. Qian, L. Wray, Y. Xia, Y. S. Hor, R. J. Cava, and M. Z. Hasan, A topological Dirac insulator in a quantum spin Hall phase, Nature (London) **452**, 970 (2008).

[17] D. Hsieh, Y. Xia, D. Qian, L. Wray, J. H. Dil, F. Meier, J. Osterwalder, L. Patthey, J. G. Checkelsky, N. P. Ong, A. V. Fedorov, H. Lin, A. Bansil, D. Grauer, Y. S. Hor, R. J. Cava, and M. Z. Hasan, A tunable topological insulator in the spin helical Dirac transport regime, Nature (London) **460**, 1101 (2009).

[18] H. Zhang, C.-X. Liu, X.-L. Qi, X. Dai, Z. Fang, and S.-C. Zhang, Topological insulators in Be_2Se_3, Bi_2Te_3 and Sb_2Te_3 with a single Dirac cone on the surface, Nat. Phys. **5**, 438 (2009).

[19] C. Liu, G. Bian, T.-R. Chang, K. Wang, S.-Y. Xu, I. Belopolski, I. Miotkowski, H. Cao, K. Miyamoto, C. Xu, C. E. Matt,

T. Schmitt, N. Alidoust, M. Neupane, H.-T. Jeng, H. Lin, A. Bansil, V. N. Strocov, M. Bissen, A. V. Fedorov, X. Xiao, T. Okuda, Y. P. Chen, and M. Z. Hasan, Tunable spin helical Dirac quasiparticles on the surface of three-dimensional HgTe, Phys. Rev. B **92**, 115436 (2015).

[20] M. Bianchi, D. Guan, S. Bao, J. Mi, B. B. Iversen, P. D. C. King, and P. Hofmann, Coexistence of the topological state and a two-dimensional electron gas on the surface of Be_2Se_3, Nat. Commun. **1**, 128 (2010).

[21] M. S. Bahramy, P. D. C. King, A. de la Torre, J. Chang, M. Shi, L. Patthey, G. Balakrishnan, Ph. Hofmann, R. Arita, N. Nagaosa, and F. Baumberger, Emergent quantum confinement at topological insulator surfaces, Nat. Commun. **3**, 1159 (2012).

[22] E. Pallecchi, A. C. Betz, J. Chaste, G. Fève, B. Huard, T. Kontos, J.-M. Berroir, and B. Plaçais, Transport scattering time probed through rf admittance of a graphene capacitor, Phys. Rev. B **83**, 125408 (2011).

[23] G. Bastard, *Wave Mechanics Applied to Semiconductor Heterostructures*, Monographies de Physique (Les Éditions de Physique, France, 1996).

[24] Y. Baum, J. Böttcher, C. Brüne, C. Thienel, L. W. Molenkamp, A. Stern, and E. M. Hankiewicz, Self-consistent kp calculations for gated thin layers of three-dimensional topological insulators, Phys. Rev. B **89**, 245136 (2014).

[25] C. Brüne, C. X. Liu, E. G. Novik, E. M. Hankiewicz, H. Buhmann, Y. L. Chen, X. L. Qi, Z. X. Shen, S. C. Zhang, and L. W. Molenkamp, Quantum Hall Effect from the Topological Surface States of Strained Bulk HgTe, Phys. Rev. Lett. **106**, 126803 (2011).

[26] D. A. Kozlov, Z. D. Kvon, E. B. Olshanetsky, N. N. Mikhailov, S. A. Dvoretsky, and D. Weiss, Transport Properties of a 3D Topological Insulator based on a Strained High-Mobility HgTe Film, Phys. Rev. Lett. **112**, 196801 (2014).

[27] Y. Guldner, C. Rigaux, M. Grynberg, and A. Mycielski, Interband Magneto-absorbtion in HgTe, Phys. Rev. B **8**, 3875 (1973).

[28] K. Bendias, R. Schlereth, C. Brüne, and H. Buhmann (unpublished).

[29] J. Baars and F. Sorger, Reststrahlen spectra of HgTe and $Cd_xHg_{1-x}Te$, Solid State Commun. **10**, 875 (1072).

[30] *Mercury Cadmium Telluride: Growth, Properties and Applications*, edited by P. Capper and J. Garland (Wiley, New York, 2010).

[31] D. Neumaier (private communication).

[32] S. Xu, Y. Han, X. Chen, Z. Wu, L. Wang, T. Han, W. Ye, H. Lu, G. Long, Y. Wu, J. Lin, Y. Cai, K. M. Ho, Y. He, and N. Wang, Van der Waals epitaxial growth of atomically thin Be_2Se_3 and thickness-dependent topological phase transition, Nano Lett. **15**, 2645 (2015).

[33] D. A. Kozlov, D. Bauer, J. Ziegler, R. Fischer, M. L. Savchenko, Z. D. Kvon, N. N. Mikhailov, S. A. Dvoretsky, and D. Weiss, Probing Quantum Capacitance in a 3D Topological Insulator, Phys. Rev. Lett. **116**, 166802 (2016).

[34] K. Nomura and A. H. MacDonald, Quantum Transport of Massless Dirac Fermions, Phys. Rev. Lett. **98**, 076602 (2007).

[35] D. Culcer, E. H. Hwang, T. D. Stanescu, and S. Das Sarma, Two-dimensional surface charge transport in topological insulators, Phys. Rev. B **82**, 155457 (2010).

[36] Q. Wilmart, A. Inhofer, M. Boukhicha, W. Yang, M. Rosticher, P. Morfin, N. Garroum, G. Fève, J.-M. Berroir, and B. Plaçais, Contact gating at GHz frequency in graphene, Sci. Rep. **6**, 21085 (2016).

[37] S. Tchoumakov, M. Civelli, and M. O. Goerbig, Magnetic description of the Fermi arc in type-I and type-II Weyl semimetals, Phys. Rev. B **95**, 125306 (2017).

[38] M. O. Goerbig, Quantum Hall effects, arXiv:0909.1998v2.

[39] E. G. Novik, A. Pfeuffer-Jeschke, T. Jungwirth, V. Latussek, C. R. Becker, G. Landwehr, H. Buhmann, and L. W. Molenkamp, Phys. Rev. B **72**, 035321 (2005).

[40] A. Inhofer, J. Duffy, M. Boukhicha, E. Bocquillon, J. Palomo, K. Watanabe, T. Taniguchi, I. Estève, J. M. Berroir, G. Fève, B. Plaçais, and B. A. Assaf, RF-quantum capacitance of topological insulator Bi_2Se_3 in the bulk depleted regime, arXiv:1707.01657v1.

[41] V. Lukose, R. Shankar, and G. Baskaran, Novel Electric Field Effects on Landau Levels in Graphene, Phys. Rev. Lett. **98**, 116802 (2007).

[42] The resurgence of a bulk contribution in the vicinity of a Dirac point is expected however, due to the vanishing Dirac screening at neutrality, illustrated by the divergence of the effective screening length $\lambda = \varepsilon/C_Q$. Such effects have been recently demonstrated in gated graphene-on-metal contacts [36]. The analog of TIs would be the case of graphene on semiconductor, where the finite compressibility of the small-gap semiconductor is taken into account. This case is beyond the scope of our paper, which focuses on the high-field regime. In the following, we shall therefore focus on the electron-doped regime and subtract a background compressibility, $\sim$0.01 Fm^{-2}.